A Study on a Compact Coupler between an Optical Fiber and a Grating-assisted Graphene-embedded Silicon Waveguide for a Wavelength-selective Photodetector

Hyungjun Heo and Sangin Kim*

Department of Electrical and Computer Engineering, Ajou University, Suwon 16499, Korea

We proposed an integrated wavelength-selective photodetector based on a grating-assisted contra-directional coupler and a graphene absorption layer for a coarse wavelength division multiplexing (CWDM) communication system. The center wavelength of the absorption spectrum of the proposed device can be tuned simply by changing the period of the grating, and the proposed device structure is suitable to forming a cascaded structure. Therefore, an array of the proposed device of different grating periods can be used for simultaneous wavelength demultiplexing and signal detection in a CWDM communication system. Our theoretical study showed that the designed device with a grating length of 500 μm could have an absorption of 95.1%, an insertion loss of 0.2 dB, and a 3 dB bandwidth of 7.5 nm, resulting in a -14 dB crosstalk to adjacent CWDM channels. We believe that the proposed device array can provide a compact and economic solution to receiver implementation in the CWDM system by combining functions of wavelength demultiplexing and signal detection.

I. INTRODUCTION

A coarse wavelength division multiplexing (CWDM) system requires a wavelength demultiplexing function as well as an optical signal detection function to implement a receiver. Considering that the CWDM system is usually a more economic solution than a dense WDM system, a more economic implementation of its receiver is desirable. As for the wavelength demultiplexing function, many solutions have been studied, which include an arrayed waveguide grating (AWG) [1], a DBR-filter [2], a microring resonator [3], and a grating-assisted coupler [4-8]. Among these, the grating-assisted asymmetric waveguide directional coupler [9] is useful in that the structure is simple compared to other filter structures and the coupling efficiency can be effectively controlled depending on a grating length. In particular, a contra-direction coupler is more advantageous than a co-directional coupler because the former is more

fabrication process tolerant: its performance is less sensitive to the grating length variation since there is no re-coupling [10]. As an effort to combine the signal detection function with the wavelength-multiplexing function for a simplified receiver, wavelength-selective photodetectors have been suggested in previous studies, which include a grating-assisted co-directional coupler with a III-V absorption layer [11] and an anti-resonant reflective optical waveguide (ARROW) structure with a quantum well (QW) absorption layer [12]. These structures have rather long coupling lengths (~1 mm), require a complicated fabrication process, and more importantly, are not compatible with Si-photonic devices.

In this paper, we propose a wavelength-selective photodetector based on a grating-assisted contra-directional coupler with a graphene absorption layer. The proposed device consists of a side-polished fiber and a silicon waveguide with a uniform grating and monolayer graphene. In general, an introduction of an absorbing layer in wavelength filters

---

changes the central wavelength and the bandwidth of the filters, and degrades the filter efficiency. Whereas, graphene with monoatomic thickness is a good candidate for absorbing material in waveguide-type filter devices because it has little effect on the properties of the filter in spite of high absorption. Graphene has been widely studied for fast broadband photodetectors because of its wide absorption bandwidth from the visible to the far infrared region and high carrier mobility [13-16]. Recently, there also have been a lot of studies on other optical devices such as polarizers [17, 18], modulators [19, 20], and exotic sensors [21] based on the tunable plasmonic effect in graphene. We have studied theoretically the feasibility of the proposed device and have shown that an array of the proposed devices of different grating periods can be used for receivers in a CWMD system which have combined functions of wave-length demultiplexing and signal detection. According to our investigation, a properly designed device of a 500 µm long grating region has a sufficiently high absorption efficiency (95.1%). We believe that the proposed device can be a compact and economic solution to the CWDM receiver implementation because of the small device size and its simple Si-photonics compatible structure.

II. THEORY

Figure 1 shows the proposed wavelength-selective photo-detector structure, which consists of a side-polished optical fiber and a silicon waveguide with a uniform grating and monolayer graphene. Figure 1(a) presents an array of photo-detectors with various resonant wavelengths for wavelength channel demultiplexing and optical signal detection. Figure 1(b) shows the cross-sectional view of a single device structure. If the silicon waveguide supports only a single guided-mode, two supermodes are formed by the coupling between the modes of the fiber and the silicon waveguide. Due to the large index difference between the fiber's core and the silicon, those two supermodes usually have very

asymmetric field distributions in the vertical direction: one has a field profile that is concentrated in the fiber's core and the other has a field profile that is concentrated in the silicon. They also show a large difference in their effective indices, which results in huge phase mismatch and thus, hinders direct coupling between them without a grating structure. Therefore, the grating on the silicon waveguide with an appropriate period enables wavelength-selective phase matching and coupling of those two supermodes. That is, the light input to the fiber is coupled to the silicon waveguide at the wavelength where the phase matching condition by the grating is satisfied, and is absorbed by the graphene layer located below the silicon waveguide. In this work, a TE wave, which has a horizontal (z direction) electric field, was considered as the incident light. Since the graphene layer is located just beneath the silicon waveguide, the supermode concentrated in the silicon experiences much higher loss than the one concentrated in the core of the fiber. According to our calculation, which be shown later, the propagation length of the supermode concentrated in the silicon has ~100,000 times shorter than that of the other supermode. This implies that light passing through the core of the fiber is hardly absorbed, and only at the wavelength of the coupling to the silicon waveguide, light is absorbed into the graphene layer. Electron-hole pairs generated by the light absorbed in monolayer graphene make electric currents by a field-effect transistor formed by two horizontally arranged electrodes (source and drain) as shown in Fig. 1(a).

Prior to the detailed design of the device, modal analysis was performed to find out a proper range of the silicon waveguide thickness. We investigated the characteristics of the supermode caused by the coupling between the two guided modes of the fiber and the silicon waveguide. For the mode calculation, a uniform silicon waveguide without a grating was assumed, and a Finite element method (FEM) based commercial tool (COMSOL) was used. A standard single mode fiber was assumed: a core diameter (t_{SMF}) of 8.2 µm and 0.36% index difference between the core and
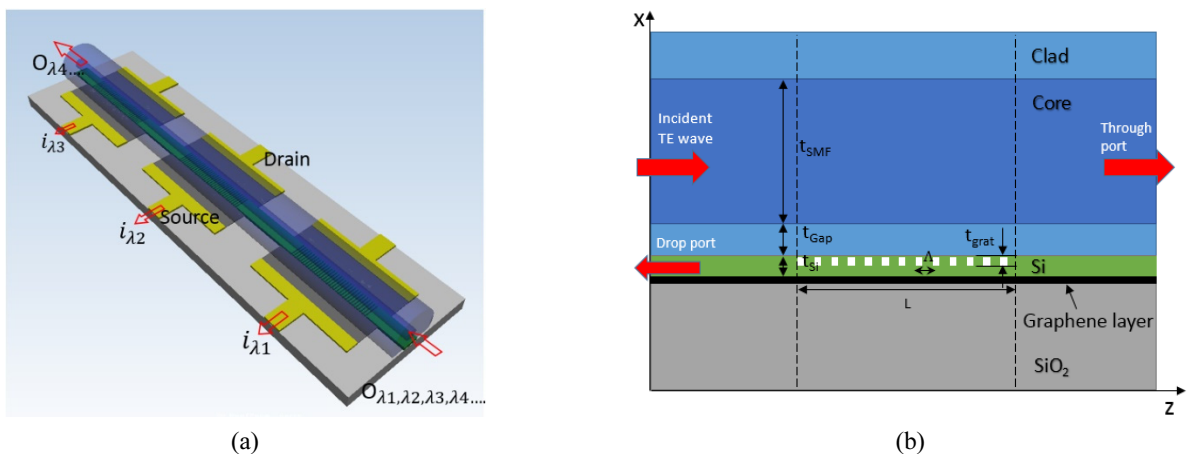

(a)   (b)

FIG. 1. (a) Schematic of an array of photodetectors with various wavelengths. (b) Cross- section view of the proposed device structure.

the cladding were assumed. The gap distance (t_{gap}) between the fiber's core and the silicon waveguide was set to be 500 nm. The complex refractive index of monolayer graphene, which was used as an absorbing layer, was calculated by $n(\lambda) = 3.0 + j\left(\dfrac{C_1}{3}\right)\lambda$, where $C_1 = 5.446$ μm^{-1} and λ was a wavelength in μm [22]. This equation was the extracted from experimental data. The refractive indices of silicon and SiO$_2$ were 3.445 and 1.444, respectively.

Figure 2(a) shows the effective index of the supermodes with the change of silicon waveguide thickness at the wavelength of 1550 nm. The supermodes were numbered according to the number of null points in their electric field distributions: mode$_0$ has no null point and mode$_1$ has one. When the silicon waveguide is thin (~15 nm), the effective index of the silicon waveguide is very close to that of the fiber, so that two fundamental modes of individual waveguides interact strongly and the effective indices of the supermodes differ from those of the fundamental modes as shown in the inset of Fig. 2(a), an enlarged view of the region where the silicon thickness is ~15 nm. The strong interaction also results in rather severe deformation of the field profiles of the supermodes as shown in Fig. 2(b). In this case, if light is launched from the single-mode fiber to the device, both of the supermodes will be excited and the

part of the incident light will be directly coupled to the silicon waveguide. This is undesirable for the wavelength-selective device operation as aforementioned. Moreover, the mode profile mismatch between the fiber mode and mode$_1$ will result in a large insertion loss. On the other hand, as the silicon waveguide becomes thick, the interaction between the individual waveguides becomes weak because of their increased effective index difference, so that the effective indices of the supermodes are very close to those of the individual fundamental modes. Figure 2(c) shows the electric field distributions of the supermodes when the silicon waveguide is 130 nm thick. The field distributions of mode$_0$ and mode$_1$ are quite similar to those of the silicon wave-guide and the fiber, respectively. Therefore, the incident light launched from the single-mode fiber will mainly excite mode$_1$ and the insertion loss will be relatively small. More importantly, the direct coupling of the incident light to the silicon waveguide will be prevented as desired. So, a rather thick silicon waveguide is needed. However, if the silicon waveguide is too thick, higher-order guided-modes will appear. Figure 2(d) shows the electric field distributions of the supermodes when the silicon waveguide is 255 nm thick. While the characteristics of mode$_0$ remains the same, the field distribution of mode$_1$ is deformed in the region of the silicon waveguide, and more importantly, a new super-
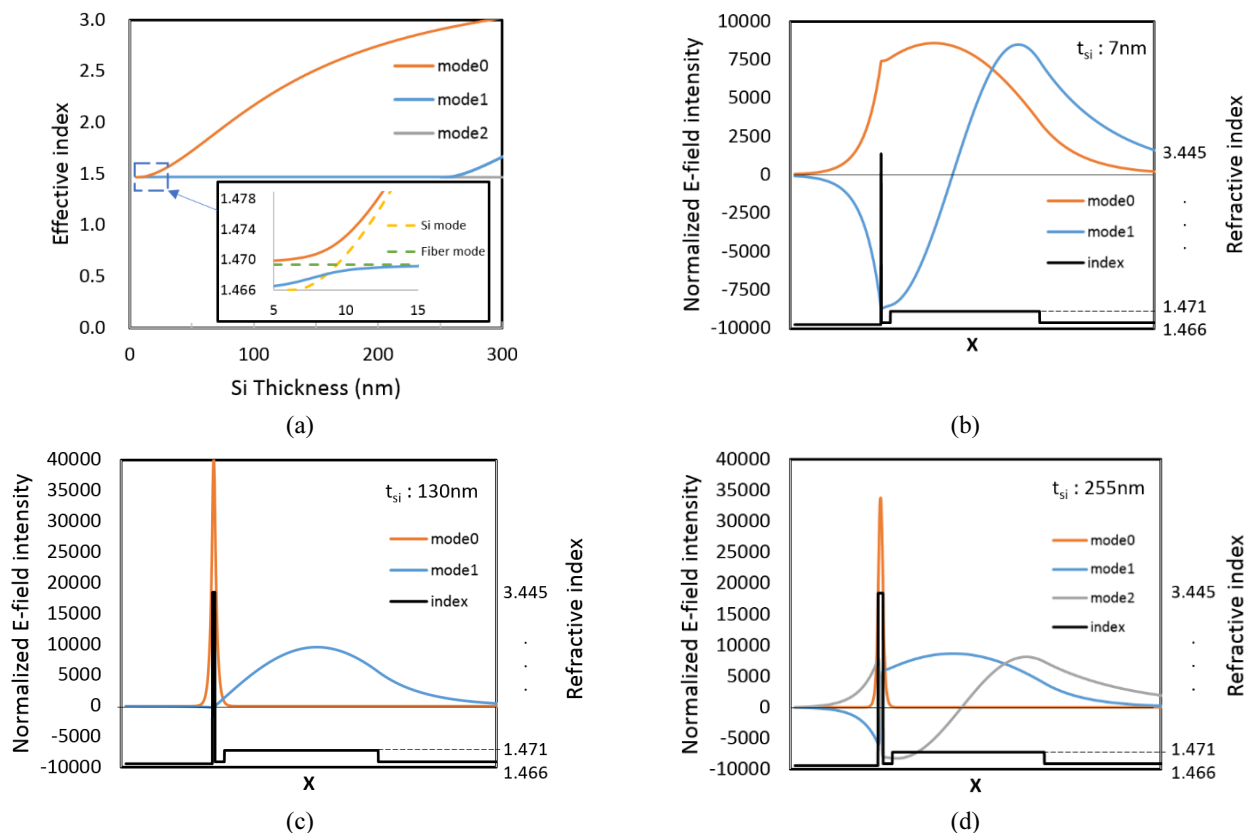

FIG. 2. Modal analysis of the proposed structure without grating. (a) Calculated the effective indices of the supermodes as a function of the silicon thickness at the wavelength of 1550 nm. The inset is the enlarged view of thin silicon thickness (the blue dotted box). (b-d) the electric distributions of each supermode for the silicon thick of 7 nm, 130 nm, and 255 nm, respectively.

mode (mode$_2$), which results from the interaction between the fundamental mode of the fiber and the second order guide-mode of the silicon waveguide, appears, whose field distribution has considerably large overlap with that of the fundamental fiber mode. This is undesirable as afore-mentioned. So, too thick silicon waveguide should also be avoided. Figure 3(a) shows the cutoff wavelengths of mode$_1$ and mode$_2$ as a function of the silicon waveguide thickness. Since the existence of mode$_2$ will cause unwanted direct coupling of the incident light to the silicon waveguide, its cutoff wavelength should lie below the wavelength range of our interest, i.e., 1470 nm $< \lambda <$ 1610 nm (corresponding to 8 CWDM channels), which is represented as a shaded region in Fig. 3(a). This limits the allowed silicon waveguide thickness to a range 5 nm to 219 nm. Figure 3(b) shows the insertion loss as a function of the silicon waveguide thickness, which was calculated from the mode overlap integral between the mode of the standard single-mode fiber and mode$_1$. A low insertion loss of approximately 0.01 dB or less is obtained when the silicon waveguide thickness lies in a range from 85 nm to 241 nm. Therefore, considering the higher-order mode avoidance and the acceptably low insertion loss, a proper range of the silicon waveguide thickness appears to be from ~85 nm to ~219 nm.

In the mode calculation, the propagation losses of the supermodes due to the graphene layer beneath the silicon waveguide were also investigated, which are not shown here. When the silicon waveguide thickness lies in the range from 50 nm to 200 nm, the loss of mode$_0$ is about 10^5 times higher than that of mode$_1$. For example, when the silicon waveguide is 100 nm thick, attenuation coefficients (α) of mode$_0$ and mode$_1$ are, respectively, ~3.06×10^{-2} μm^{-1} and ~1.39×10^{-7} μm^{-1}, corresponding to propagation lengths of 32.6 μm and 7.21 m. So, the loss of mode$_1$ does not play an important role, and the relatively short propagation length of mode$_0$ guarantees almost complete absorption of the light coupled to the silicon waveguide.

In the modal analysis above, we assumed a semi-infinite SiO$_2$ substrate. In practice, the SiO$_2$ substrate thickness should be finite. Moreover, an SiO$_2$ layer of a finite thickness deposited or grown on a silicon substrate may be adopted to fully exploit the silicon photonics compatibility of the proposed structure for economic fabrication. So, we also investigated the effect of the finite SiO$_2$ layer thickness in both cases. In the SiO$_2$ substrate case, the guided super modes become stable when the substrate is thicker than 1.0 μm. In the silicon substrate case, an SiO$_2$ layer thicker than 1.0 μm is also enough to not affect the guided super-modes. Therefore, in all the calculations shown later in this paper, a 2.0 μm thick SiO$_2$ layer is assumed for safe elimination of the finite substrate thickness effect. If other materials whose indices are higher than that of SiO$_2$ are used, the required thickness of the lower clad will be larger in the silicon substrate case.

For more efficient device design base on numerical calculations, the proposed structure is also modeled by the coupled-mode theory (CMT) with an assumption that the direct coupling between the supermodes is prevented. The phase matching condition for compensation of the phase difference between two supermodes with a grating given by

$$\Delta\beta_{01} = \beta_0 - (\pm \beta_1) - \frac{2\pi}{\Lambda} = 0, \qquad (1)$$

where β_i represent the propagation constant of the mode$_i$, Λ is a period of the grating, and the sign in the parentheses indicates the propagation direction: + is for the forward direction and − is for the reverse direction. In other words, if − (+) is chosen in the parentheses, contra (co)-directional coupling of two supermodes occurs at the wavelengths satisfying Eq. (1). One can see that the required grating period for the contra-directional coupling is always smaller than that of the co-directional one. A smaller grating period makes the whole device length shorter for the same
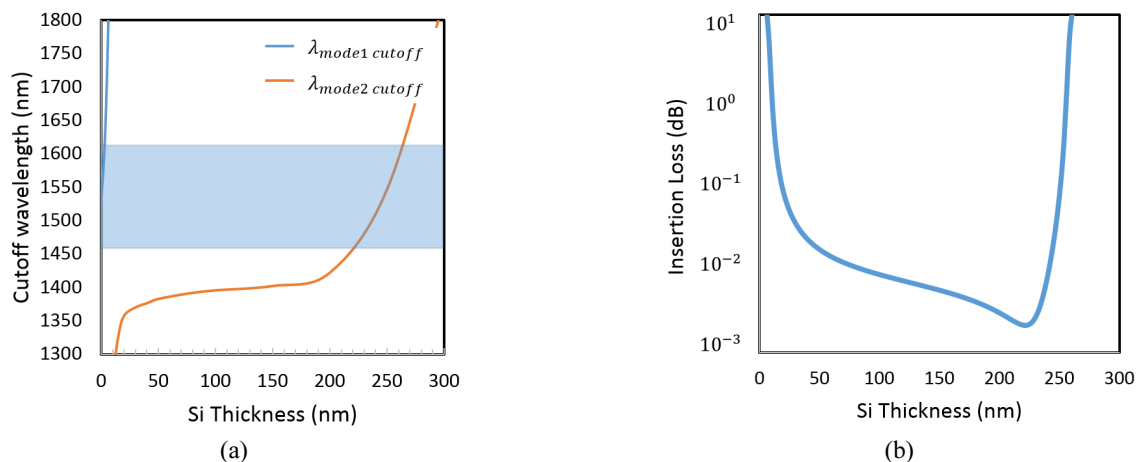

FIG. 3. (a) The cutoff wavelength of mode$_1$ and mode$_2$ and (b) the insertion loss as a function of the silicon waveguide thickness. The shaded box in (a) presents the wavelength range of 8 CWDM channels.

number of gratings. In addition, since the smaller grating period causes less unwanted scattering at a given operating wavelength, so that the characteristics of the wavelength-selective directional coupler are maintained even for the deeper grating. As will be explained later, the deep grating enhances the coupling coefficient (κ_{01}), which reduces the device length for a given absorption efficiency. Therefore, in this work, we considered only the design of the contra-directional coupler based integrated photodetector. The Bragg reflection condition of a grating in which each excited supermode is reflected back to its own mode of the counter propagation direction is given by

$$\Delta\beta_{0,1} = \beta_{0,1} - \frac{\pi}{\Lambda} = 0. \qquad (2)$$

However, in the proposed device scheme, this Bragg reflection should be avoided because it creates unnecessary energy loss and noise. Figure 4 shows the phase matching conditions graphically when the silicon waveguide is 100 nm thick and $\Lambda = 426$ nm. The mode$_0$-mode$_1$ coupling occurs at $\lambda_{couple} = 1550\ nm$, while the Bragg reflections of mode$_0$ and mode1 occur at $\lambda_{mode_0} = 1275\ nm$ and $\lambda_{mode_1} = 1770\ nm$, respectively.

Since the Bragg reflection wavelengths are sufficiently far apart from the wavelength range of our interest, we can ignore the self-reflection terms in the CMT modeling. Therefore, coupled mode equations [23, 24] of two waveguides can be simplified as follows:

$$\frac{dA^+}{dz} = -j\kappa_{01}B^- e^{j(\Delta\gamma_0 + \Delta\gamma_1)z} \qquad (3a)$$

$$\frac{dB^-}{dz} = j\kappa_{01}^* A^+ e^{-j(\Delta\gamma_0 + \Delta\gamma_1)z}, \qquad (3b)$$
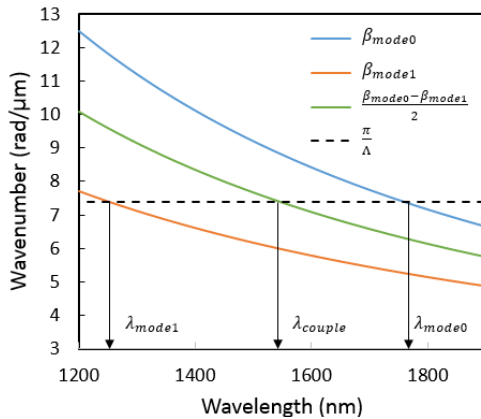

FIG. 4. Propagation constant calculated by modal analysis to show the phase matching conditions graphically when the silicon waveguide is 100 nm thick. For a grating period of 426 nm designed to have $\lambda_{couple} = 1550\ nm$, each Bragg reflection wavelength is $\lambda_{mode_0} = 1275\ nm$ and $\lambda_{mode_1} = 1770\ nm$, respectively.

where A and B are the amplitudes of the supermodes, the superscripts (+, −) indicate propagation directions (forward or backward), and $\Delta\gamma_i = \Delta\beta_i \pm j\alpha_i$ is a complex propagation constant (the attenuation coefficient is positive in the forward direction and negative in the backward direction). The coupling coefficient (κ_{01}) is calculated as

$$\kappa_{01} = \kappa_{01}^* = \frac{\omega}{4}\int_{-\infty}^{\infty} E_{mode1}(x)\Delta\varepsilon(x)E_{mode0}(x)dx, \qquad (4)$$

where $\Delta\varepsilon(x)$ is the dielectric perturbation in a grating, ω is an angular frequency, and $E_{mode\,i}$ is the electric field distribution of the supermode. The solution of the coupled mode equation is given by

$$B(z) = A_0\frac{j\kappa_{01}\sinh(S(z-L))e^{j(\Delta\gamma_1 - \Delta\gamma_0)z/2}}{-\Delta\gamma_{01}\sinh(SL) + jScosh(SL)} \qquad (5)$$

$$A(z) = A_0\frac{j(\Delta\gamma_{01}\sinh(S(z-L)) + jScosh(S(z-L)))e^{j(\Delta\gamma_1 - \Delta\gamma_0)z/2)}}{-\Delta\gamma_{01}\sinh(SL) + jScosh(SL)}, \qquad (6)$$

where $\Delta\gamma_{01} = (\Delta\gamma_0 + \Delta\gamma_1)/2$, $S = \sqrt{\kappa_{01}^2 - \Delta\gamma_{01}^2}$, and A_0 and L are a modal amplitude of an incident wave and a grating length, respectively. The throughput transmission in the fiber core and the drop efficiency in the silicon waveguide are represented by $\eta_{through} = |A^+(L)|^2/|A^+(0)|^2$ and $\eta_{drop} = |B^-(0)|^2/|A^+(0)|^2$, respectively. Due to the substantial loss of mode$_0$ mainly guided in the silicon waveguide, the wave propagating through the drop port is also absorbed into the graphene layer within a short length. Thus, the final graphene absorption efficiency can be simply calculated $\eta_{absorption} = 1 - \eta_{through}$.

III. DESIGN

In designing the proposed device, design parameters include a silicon waveguide thickness (t_{Si}), a grating depth (t_{grat}), a grating period (Λ), and a grating length (L). The main goal of our design is to minimize the device (or grating) length for a sufficiently high absorption efficiency (> 95%). In most of the design process, the clad thickness (t_{gap}) between the fiber core and the silicon waveguide was set to be 500 nm considering the fabrication tolerance in side-polishing of the fiber. The effect of t_{gap} variation was also examined. All the calculations in this work were conducted by using the commercial FEM tool (COMSOL), which were confirmed by comparing with the CMT analysis described in Section II. The same material constants that were used in the mode analysis in Section II were used in all the calculations.

First, the influence of the grating depth (t_{grat}) was investigated for silicon thicknesses of $t_{Si} = 100$ nm, 130 nm

and 160 nm. Figure 5(a) shows the coupling coefficient (κ_{01}) as a function of the grating depth. The coupling coefficient is determined by the electric field distribution of the two supermodes in the grating area as shown in Eq. (4). However, Eq. (4) is valid for small perturbation of the dielectric constant of the grating. For a deep grating of high index contrast, it is difficult to calculate the coupling coefficient accurately by an analytical method. In this work, we estimated the coupling coefficient by fitting the CMT result derived in section II with the absorption and transmission spectra calculated with the FEM at a specific grating length (L = 100 μm). The validity of the estimation was confirmed by comparing the FEM calculated spectra for other grating lengths with the CMT results based on the estimated coupling coefficient. As will be shown later, those two calculations agree well up to L = 1000 μm, which is long enough to obtain a sufficiently high absorption efficiency (>95%). In Fig. 5(a), one can see that the coupling coefficient monotonically increases with the grating depth

when t_{Si} = 100 nm and 130 nm. Whereas, when t_{Si} = 160 nm, the coupling coefficient decreases to zero at a grating depth of ~37% and increases again. This can be understood from the electric field distribution of mode$_1$. Figure 5(b) shows the electric field distributions of mode$_1$ for various t_{Si}. The inset is an enlarged view near the boundary between the silicon waveguide and the clad of the fiber which is represented by the red dotted line. As the thickness of the silicon increases, the null point at which the sign of the electric field changes shifts into the silicon waveguide. On the other hand, the field distribution of mode$_0$ remains almost the same for the considered values of t_{Si}. So, when the null point of mode$_1$ lies in the silicon waveguide (for example, when t_{Si} = 160 nm), the overlap integral between mode$_0$ and mode$_1$ can be zero for a certain grating depth. The mode overlap integral also explains why the thinner silicon waveguide has the larger coupling coefficient for the same relative grating depth. According to our investigation, when t_{Si} < 100 nm the, coupling

(a)

(b)

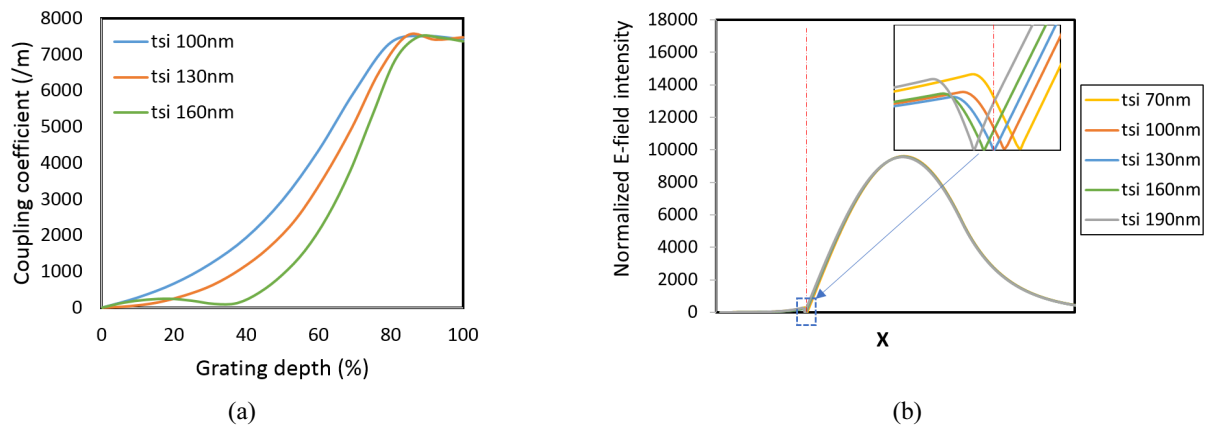FIG. 5. (a) Coupling coefficient as a function of grating depth for t_{Si} = 100 nm, 130 nm, and 160 nm. (b) Electric field distribution of mode$_1$ for various silicon thicknesses from 70 nm to 190 nm. The red dotted line represents a boundary of the silicon layer and the clad of the fiber.
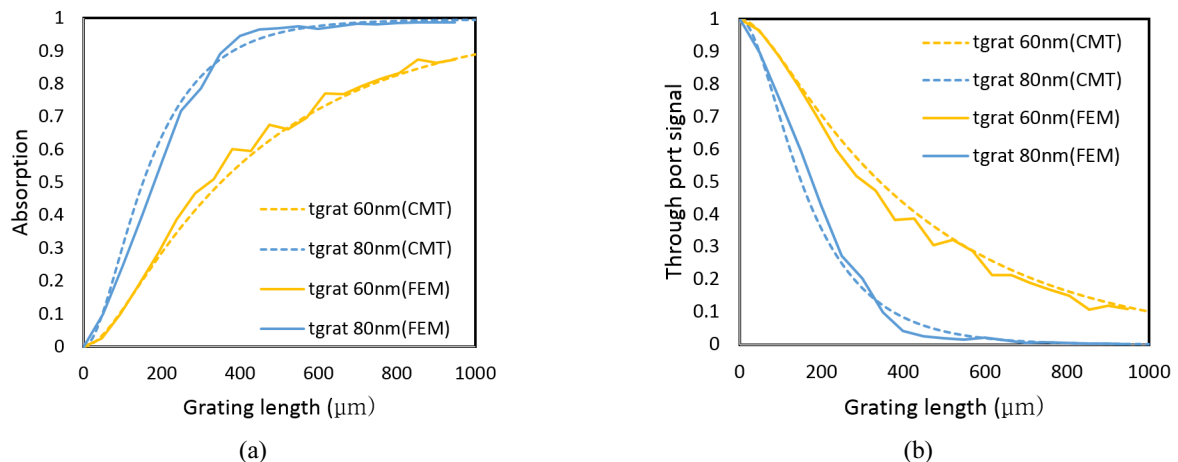

(a)

(b)

FIG. 6. (a) Peak absorption efficiencies and (b) transmissions at the through port as a function of a grating length (L) when t_{Si} = 100 nm with t_{grat} = 60 nm and 80 nm. Each result was calculated by the FEM (solid line) and the CMT (dotted line).

coefficient increases further for a small relative grating depth, but the maximum allowed grating depth becomes smaller. As a result, the maximum achievable coupling coefficient remains about the same as the case of $t_{Si} = 100$ nm. Therefore, considering either insertion loss and coupling coefficient (or device length), $t_{Si} = 100$ nm appeared to be a proper choice. When the relative grating depth is above 80%, the coupling coefficients remain the same for all t_{Si}. We surmise that this is because the increased scattering of the deep grating partially destroys the guiding of the silicon layer. Coupling effect is restricted. So, as for the relative grating depth, 80% appears to be a proper choice.

Figure 6 shows peak absorption efficiencies and transmissions at the through port as a function of grating length (L) when $t_{Si} = 100$ nm with $t_{grat} = 60$ nm and 80 nm. The grating periods were chosen to have the peak absorption at a wavelength of 1550 nm: $\Lambda = 474$ nm for $t_{grat} = 60$ nm and $\Lambda = 499$ nm for $t_{grat} = 80$ nm. The solid lines show the FEM calculations and the dotted lines show the CMT results with the estimated coupling and the attenuation coefficients. Note that the attenuation coefficient (α) is estimated simultaneously with the coupling coefficient in the aforementioned fitting process. In general, the FEM calculations agree well with the CMT results. As mentioned earlier, the coefficients estimated for $L = 100$ μm were used for all the other grating lengths, which confirms the validity of the CMT modeling of our device. We surmise that the ripple in the FEM results from Fabry-Perot resonance due to the reflections at the ends of the grating region. For an absorption efficiency of 95%, a grating length of about 500 μm (~1.4 mm) is required when the grating depth is 80 nm (60 nm). This can be understood from the coupling coefficients: for $t_{grat} = 60$ nm and 80 nm, $\kappa_{01} = 4349$ m^{-1} and for $t_{grat} = 80$ nm, $\kappa_{01} = 7340$ m^{-1}, respectively, as shown in Fig. 5(a). In the proposed device, the loss of $mode_0$ is very high, so that the attenuation coefficient is much larger than the coupling coefficient. This implies that one the incident wave carried by $mode_1$ is coupled to $mode_0$, it is quickly absorbed by the graphene layer. Therefore, the absorption efficiency is mainly determined by the magnitude of the coupling coefficient for a fixed grating length.

Figure 7(a) shows absorption and transmission (at the through port) spectra for $t_{grat} = 80$ nm and 100 nm with $t_{Si} = 100$ nm, and $L = 500$ μm. The grating period was chosen such that a peak absorption occurs at the wavelength of 1550 nm in each case: $\Lambda = 499$ nm for $t_{grat} = 80$ nm and $\Lambda = 523$ nm for $t_{grat} = 100$ nm. Since the coupling coefficient remains almost the same for $t_{grat} > 80\%$ as shown in Fig. 5(a), the absorption spectra for $t_{grat} = 80$ nm and 100 nm are similar in general. The maximum absorption efficiency of 95.1% and the 3 dB bandwidth of 7.5 nm were obtained. Owing to the stronger scattering, the case of $t_{grat} = 100$ nm shows ripples at the short wavelengths, where absorption is less than 10%. This scattering effect causes crosstalk of ~10 dB to the adjacent wavelength channels. In order to avoid such a scattering effect, the grating depth of 80 nm

is more desirable. The black dotted curve represents the CMT result with $\kappa_{01} = 7340$ m^{-1}, which agrees well with the FEM calculation. The spectrum of the transmission at the through port for $t_{grat} = 80$ nm is also plotted in Fig. 7(a), which demonstrates that the unwanted scattering of the grating is negligible, so that all the unabsorbed wave appears as the transmission at the through port with an insertion loss of 0.2 dB. Figures 7(b) and 7(c) show the electric field distributions (cross-section view at the center) when the TE wave is incident on the core of the fiber. At $\lambda = 1550$ nm (Fig. 7(b)), most of the incident wave is coupled to the silicon waveguide and absorbed into graphene. On the contrary, at $\lambda = 1530$ nm (Fig. 7(c)), most of the incident wave propagates through the fiber core with no coupling to the silicon waveguide.
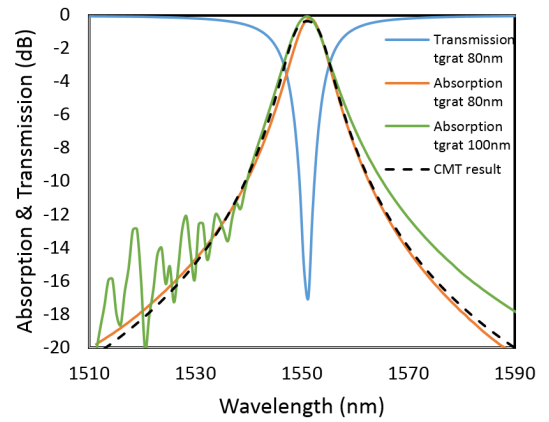
(a)
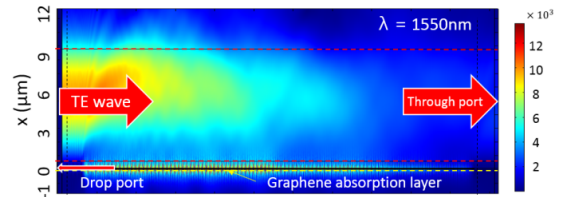
(b)
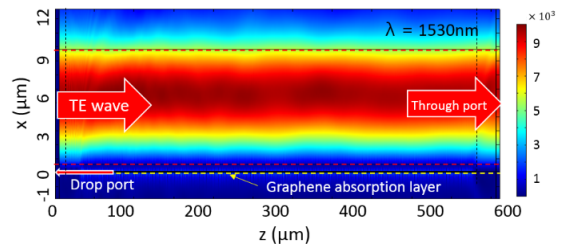
(c)

FIG. 7. (a)Absorption spectra for grating depth of 80 nm and 100 nm with L = 500 μm, $t_{Si} = 100$ nm, $\Lambda = 499$ nm and 523 nm for $\lambda_{couple} = 1550$ nm, respectively. Transmission spectrum for $t_{grat} = 80$ nm and CMT results with $\kappa_{01} = 7340$ m^{-1} are also added as a solid blue line and a dotted black line, respectively. (b, c) Cross-sectional views of electric field distributions when the wavelength of an incident TE wave are 1550 nm and 1530nm, respectively, for $t_{grat} = 80$ nm.
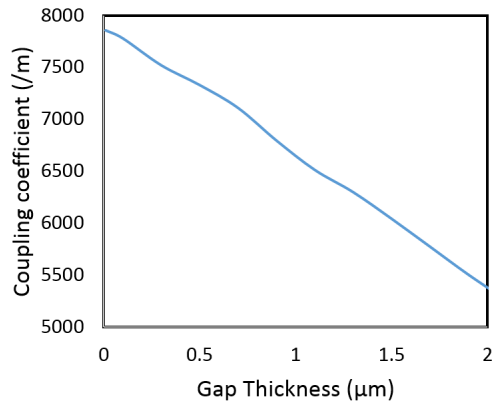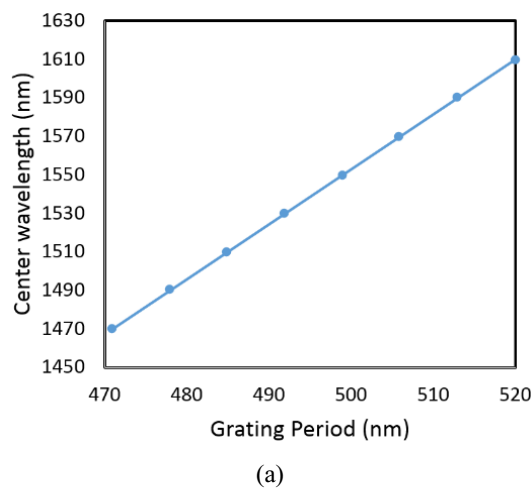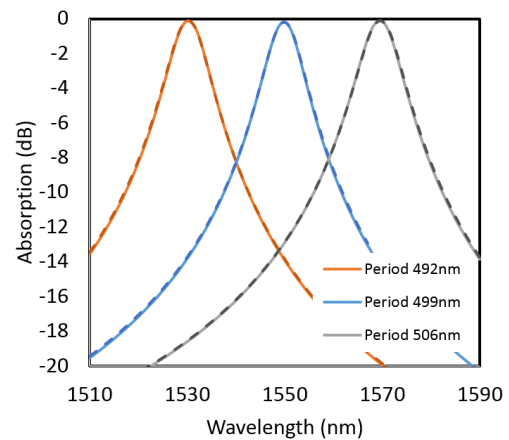
FIG. 8. Coupling coefficient as a function of a gap distance between the fiber core and the silicon waveguide.

We also investigated the influence of the thickness of the clad between the fiber core and the silicon waveguide (t_{gap}). Figure 8 shows the coupling coefficient as a function of t_{gap} for $t_{Si} = 100$ nm, $t_{grat} = 80$ nm, and $\Lambda = 499$ nm. As the gap increases, the coupling coefficient shows a linear decrease because the overlap integral between the two supermodes becomes smaller. So, for a smaller t_{gap}, the higher coupling coefficient and thus, a shorter device length are obtained. However, considering fabrication tolerance during the optical fiber polishing, $t_{gap} = 500$ nm seems to be a reasonable choice.

Figure 9(a) shows the center wavelength of the absorption spectrum as a function of the grating period for $t_{Si} = 100$ nm, $t_{grat} = 80$ nm, $t_{gap} = 500$ nm. Since the supermodes of the designed structure show linear-like dispersion in the wavelength range of our interest as shown in Fig. 4, the central wavelength varies linearly with the grating period. Figure 9(b) shows the FEM calculated absorption spectra for $\Lambda = 492$ nm, 499 nm, and 506 nm designed for the center wavelengths of 1530 nm, 1550 nm, and 1570 nm, which correspond to three central wavelength channels of the CWDM. The maximum absorption efficiencies were 96.0%, 95.1%, and 95.5%, respectively. The 3 dB bandwidths were 8 nm, 7.5 nm, and 7.6 nm, respectively, which causes -14 dB crosstalk with neighboring channels. As the center wavelength shifts with a period change, spectral characteristics remain almost the same, which is a desirable feature in fabrication as well as design.

V. DISCUSSION

In this work, we used an approximate formula for the index of graphene [22]. In Fig. 10, the approximate formula is compared to Kubo formula [25, 26] that is believed to be more accurate. The approximation seems to be acceptably close to the Kubo formula in the wavelength range of our interest. In order to investigate the effect of the approximation on the device performance, the absorption spectra were calculated with the graphene index extracted from the Kubo formula and plotted in Fig. 9(b) (dotted lines). One can see that the approximation of the graphene index makes negligible difference in the device performance.

We also investigated the effect of multilayer graphene on the device performance. Figure 11 shows peak absorption efficiencies as a function of grating length(L) with bilayer and trilayer graphene used when $t_{Si} = 100$ nm, $t_{grat} = 80$ nm, and $\Lambda = 499$ nm. The index of multilayer graphene was modeled by assuming the conductivity of n-layer graphene is n times of that of monolayer graphene [27, 28]. For comparison, the absorption spectrum for the monolayer graphene case presented in Fig. 6(a) was also plotted together. As the number of graphene layers increases, the peak absorption efficiency decreases for all grating lengths. This can be explained by the CMT modeling. When $z = L$, at

(a)

(b)

FIG. 9. (a) Center wavelength as a function of grating period. (b) Absorption spectra for grating periods of 492 nm, 499 nm, and 506 nm designed for center wavelengths of 1530 nm, 1550 nm, and 1570 nm, respectively, with $t_{Si} = 100$ nm, $t_{grat} = 80$ nm, L = 500 μm. The dotted lines represent the calculated absorption spectra were with the graphene index extracted from Kubo formula.

(a)   (b)
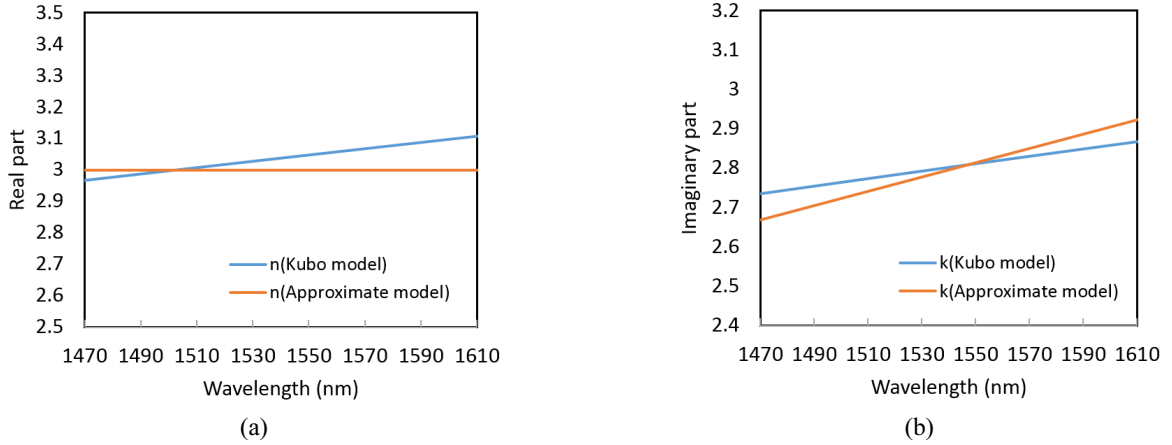
FIG. 10. Comparison between an approximate formula ($n(\lambda) = 3.0 + j\left(\dfrac{C_1}{3}\right)\lambda$, where $C_1 = 5.446$ μm^{-1} and λ was a wavelength in μm) and the Kubo formula. (a) real part and (b) imaginary part.

the wavelength of resonance (satisfying the phase matching condition, $\beta_0 - \beta_1 = 2\pi/\Lambda$), the Eq. (6) becomes

$$
|A(L)| = A_0 \frac{|S|}{|-\Delta\gamma_{01}\sinh(SL) + jS\cosh(SL)|}
$$

$$
= A_0 \frac{\sqrt{\kappa_{01}^2 + \left(\frac{\alpha_0}{2}\right)^2}}{\left| \frac{-\alpha_0}{2}\sinh\left(\sqrt{\kappa_{01}^2 + \left(\frac{\alpha_0}{2}\right)^2}\,L\right) + \sqrt{\kappa_{01}^2 + \left(\frac{\alpha_0}{2}\right)^2}\cosh\left(\sqrt{\kappa_{01}^2 + \left(\frac{\alpha_0}{2}\right)^2}\,L\right) \right|},
$$

$$(7)$$

where $\alpha_1 \ll \alpha_0$ is assumed as aforementioned. One can see that as the loss of graphene (α_0) increases, the throughput transmission ($\eta_{through} = |A^+(L)|^2/|A^+(0)|^2$) increases for a given L and thus, the absorption efficiency ($\eta_{absorption} = 1 - \eta_{through}$) should decrease. This would look counterin-

tuitive at first glance. However, it can be understood from the phase matching condition Eq. (1): the loss imbalance between those two supermodes ruins the phase matching condition and thus, the m_1-to-m_0 wave coupling through the grating as well. This implies that for a larger α_0, a larger L is needed to get a certain $\eta_{through}$, which will make the device long. It should also be noted that even for a large α_o, we can get an arbitrarily small $\eta_{through}$ by increasing L since Eq. (7) tends to zero as $L \to \infty$. The dotted lines in Fig. 11 represent the CMT calculation results with the estimated coupling and the attenuation coefficients. The estimated coupling coefficient (κ_{01}) was 7340 m^{-1} for all three cases. The estimated attenuation coefficients (α_0) were 13377 m^{-1}, 28801 m^{-1}, and 44083 m^{-1} for the cases of monolayer, bilayer, and trilayer graphene, respectively.

From Eq. (7), an optimal attenuation coefficient to minimize a device length appears to be zero. This implies that the graphene layer under the grating region should be removed and only placed in the drop port region. In this case, however, there is a huge scattering loss at the interface between the grating and the drop port waveguide ($z = 0$) for a large grating depth, which results in absorption efficiency degradation. So, the graphene layer was extended to the grating region and the scattering loss became negligible as verified in Fig. 7(b).

In this work, we assumed a TE wave as an incident wave. The attenuations of the silicon waveguide with the graphene layer for both TE and TM waves are dependent on the waveguide geometry, i.e., especially the waveguide thickness. According to our investigation, for the waveguide thickness up to ~190 nm, the attenuation of TM wave is lower than that of TE wave, and it has been found that the TM wave attenuation is too low to prevent the scattering at the interface between the grating and the drop port waveguide for a 100 nm thick waveguide. So, we focused on the TE wave case in this work.
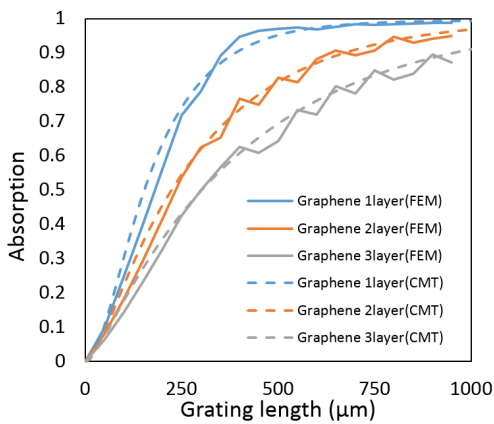

FIG. 11. Peak absorption efficiencies as a function of grating length (L) for the devices with monolayer, bilayer and trilayer graphene used when $t_{Si} = 100$ nm, $t_{grat} = 80$ nm, and $\Lambda = 499$ nm. The index of multilayer graphene was modeled by assuming the conductivity of n-layer graphene is n times of that of monolayer graphene. The dotted lines represent the CMT calculation results with the estimated coupling and the attenuation coefficients.

VI. CONCLUSION

We have proposed an integrated wavelength-selective graphene photodetector based on a grating-assisted contra-directional coupler, an array of which can be used for simultaneous wavelength demultiplexing and signal detection of CWDM channels. The proposed structure consists of a side-polished fiber and a silicon waveguide with uniform grating and monolayer graphene. The operation principle of the proposed device was studied with the guided-mode analysis and the coupled mode theory modeling. We also investigated proper ranges of geometric parameters considering their effect on the device performance. Considering an insertion loss and a device length, an optimal device structure was designed: when a silicon waveguide thickness, a grating depth, and a grating length are $t_{Si} = 100$ nm, $t_{grat} = 80$ nm, and $L = 500$ μm, respectively, a peak absorption efficiency of 95.1% and a 3 dB bandwidth of 7.5 nm were obtained at a center wavelength of 1550 nm with a grating period of $\Lambda = 499$ nm. We also demonstrated tuning of the center wavelength by changing the grating period with the device performance remained almost the same. For a CWDM application, an array of the designed wavelength-selective photodetectors will have a -14 dB crosstalk to adjacent wavelength channels. We believe that the proposed wavelength-selective photodetector array may be a compact and economic solution to the wavelength demultiplexing and signal detection in a CWDM communication system.

ACKNOWLEDGMENT

REFERENCES

1. X. J. Leijtens, B. Kuhlow, and M. K. Smit, "Arrayed wave-guide gratings," in *Wavelength Filters in Fibre Optics*, H. Venghaus, ed. (Springer, NewYork, USA, 2006).
2. T. Numai, "Semiconductor wavelength tunable optical filters," Int. J. Nonlinear Opt. Phys. **2**(4), 643-659 (1993).
3. T. Barwicz, M. A. Popovic, P. T. Rakich, M. R. Watts, H. A. Haus, E. P. Ippen, and H. I. Smith, "Microring-resonator-based add-drop filters in SiN: fabrication and analysis," Opt. Express **12**(7), 1437-1442 (2004).
4. L. Dong, P. Hua, T. A. Birks, L. Reekie, and P. S. J. Russell, "Novel add/drop filters for wavelength-division-multiplexing optical fiber systems using a Bragg grating assisted mismatched coupler," IEEE Photon. Technol. Lett. **8**(12), 1656-1658 (1996).
5. C. Riziotis and M. N. Zervas, "Design considerations in optical add/drop multiplexers based on grating-assisted null couplers," J. Lightwave Technol. **19**(1), 92-104 (2001).
6. J. P. Weber, "Spectral characteristics of coupled-waveguide Bragg-reflection tunable optical filter," IEE Proc. Optoelectron. **140**(5), 275-284(1993).
7. R. R. A. Syms, "Improved coupled-mode theory for codirectionally and contra-directionally coupled waveguide arrays," J. Opt. Soc. Am. A **8**(7), 1062-1069 (1991).
8. C. Bulmer and M. Wilson, "Single mode grating coupling between thin-film and fiber optical waveguides," IEEE J. Quantum Electron. **14**(10), 741-749(1978).
9. W. Shi, X. Wang, C. Lin, H. Yun, Y. Liu, T. Baehr-Jones, M. Hochberg, N. A. F. Jeager, and L. Chrostowski, "Silicon photonic grating-assisted, contra-directional couplers," Opt. Express **21**(3), 3633-3650(2013).
10. T. Erdogan, "Optical add-drop multiplexer based on an asymmetric Bragg coupler," Opt. Commun. **157**(1), 249-264 (1998).
11. H. Sakata, "Analysis of wavelength-selective photodetectors based on grating-assisted forward coupling," J. Lightwave Technol. **11**(4), 560-566 (1993).
12. E. Mao, D. R. Yankelevich, C. C. Lin, O. Solgaard, A. Knoesen, and J. S. Harris, "Narrow-band light emission in semiconductor-fibre asymmetric waveguide coupler," Electron. Lett. **36**(16), 1378-1379 (2000).
13. A. Pospischil, M. Humer, M. M. Furchi, D. Bachmann, R. Guider, T. Fromherz, and T. Mueller, "CMOS-compatible graphene photodetector covering all optical communication bands," Nat. Photon. **7**(11), 892-896 (2013).
14. X. Gan, R. J. Shiue, Y. Gao, I. Meric, T. F. Heinz, K. Shepard, J. Hone, S. Assefa, and D. Englund, "Chip-integrated ultrafast graphene photodetector with high responsivity," Nat. Photon. **7**(11), 883-887 (2013).
15. S. Schuler, D. Schall, D. Neumaier, L. Dobusch, O. Bethge, B. Schwarz, M. Krall, and T. Mueller, "Controlled generation of ap-n junction in a waveguide integrated graphene photo-detector," Nano Lett. **16**(11), 7107-7112 (2016).
16. R. J. Shiue, Y. Gao, Y. Wang, C. Peng, A. D. Robertson, D. K. Efetov, S. Assefa, F. H. L. Koppens, J. Hone, and D. Englund, "High-responsivity graphene-boron nitride photo-detector and autocorrelator in a silicon photonic integrated circuit," Nano Lett. **15**(11), 7288-7293 (2015).
17. X. Yin, X. Ke, L. Chen, T. Zhang, J. Li, Z. Zhu, and X. Li, "Ultra-broadband TE-pass polarizer using a cascade of multiple few-layer Graphene embedded silicon waveguides," J. Lightwave Technol. **34**(13), 3181-3187 (2016).
18. Z. H. Zhu, C. C. Guo, K. Liu, J. F. Zhang, W. M. Ye, X. D. Yuan, and S. Q. Qin, "Electrically controlling the polarizing direction of a graphene polarizer," J. Appl. Phys. **116**(10), 104304 (2014).
19. M. Kim, C. Y. Jung, H. Heo, and S. Kim, "Optical reflection modulation using surface plasmon resonance in a graphene-embedded hybrid plasmonic waveguide at optical communication wavelength," Opt. Lett. **40**, 871-874 (2015).
20. T. Q. Tran, S. Lee, and S. Kim, "Tunable wide-angle tunneling in graphene-assisted frustrated total internal reflection," Sci. Rep. **6**, 19975 (2016).
21. A. Farmani, M. Miri, and M. H. Sheikhi, "Tunable resonant Goos-Hänchen and Imbert-Fedorov shifts in total reflection of terahertz beams from graphene plasmonic metasurfaces," J. Opt. Soc. Am. B **34**(6), 1097-1106 (2017).
22. M. Bruna and S. Borini, "Optical constants of graphene layers in the visible range," Appl. Phys. Lett. **94**(3), 031901 (2009).

23. S. S. Orlov, A. Yariv, and S. V. Essen, "Coupled-mode analysis of fiber-optic add-drop filters for dense wavelength-division multiplexing," Opt. Lett. **22**(10), 688-690 (1997).
24. S. Olivier, H. Benisty, C. Weisbuch, C. J. Smith, T. F. Krauss, and R. Houdré, "Coupled-mode theory and propagation losses in photonic crystal waveguides," Opt. Express **11**(13), 1490-1496 (2003).
25. A. Farmani, M. Miri, and M. H. Sheikhi, "Analytical modeling of highly tunable giant lateral shift in total reflection of light beams from a graphene containing structure," Opt. Commun. **391**, 68-76(2017).
26. G. W. Hanson, "Dyadic Green's functions and guided surface waves for a surface conductivity model of graphene," J. Appl. Phys. **103**(6), 064302 (2008).
27. H. S. Chu and C. H. Gan, "Active plasmonic switching at mid-infrared wavelengths with graphene ribbon arrays," Appl. Phys. Lett. **102**, 231107 (2013).
28. C. Casiraghi, A. Hartschuh, E. lidorikis, H. Qian, H. Harutyunyan, T. Gokus, K. S. Novoselov, and A. C. Ferrari, "Rayleigh imaging of graphene and graphene layers," Nano Lett. **7**, 2711-2717 (2007).